Effect of Slip Boundary Conditions on the Simulation of Microparticle Velocity Fields in a Conical Fluidized Bed

Alireza Bahramian
Dept. of Chemical Engineering, Hamedan University of Technology, P.O. Box, 65155 Hamedan, Iran

Martin Olazar
Dept. of Chemical Engineering, University of the Basque Country, P.O. Box, 644, 48080 Bilbao, Spain

Goodarz Ahmadi
Dept. of Mechanical and Aeronautical Engineering, Clarkson University, Potsdam, NY 13699

DOI 10.1002/aic.14211
Published online August 23, 2013 in Wiley Online Library (wileyonlinelibrary.com)

The hydrodynamic performance of micrometric TiO_2 particles has been experimentally studied in a conical fluidized bed and the results compared with numerical simulations. Local solid velocities in the bed have been measured by means of an optical fiber technique under different operating conditions of particle loading and air velocity. The radial profiles of axial solid velocities have been simulated to assess the sensitivity of grid size, and different drag models, namely, those by Syamlal and O'Brien, Ahmadi and Ma, Arastoopour et al., and Gidaspow, for no-slip, partial-slip, and free-slip boundary conditions (BCs). The different drag models record almost similar results, but those provided by the Gidaspow and Ahmadi–Ma models, together with free-slip BCs, are in somewhat better agreement with the experimental data for conical fluidized beds with smooth walls. © 2013 American Institute of Chemical Engineers *AIChE J*, 59: 4502–4518, 2013
Keywords: conical fluidized bed, solid velocity, slip boundary conditions, numerical simulation, drag models

Introduction

Fluidized and spouted beds are extensively used for various industrial applications in pharmaceuticals,[1,2] drying,[3,4] food processing,[5] combustion,[6,7] pyrolysis, and catalytic polymerization.[8,9] A conical fluidized bed has the characteristics of both fluidized and spouted beds, being, therefore, suitable for handling agglomerating or sticky powders. This is particularly the case for the fluidization of fine particles with a wide size distribution corresponding to different groups of Geldart's classification.[10,11] Although many studies have been reported in the literature involving fluidized beds,[12–15] certain details of the hydrodynamic performance of conical fluidized beds are not fully understood, which is partially due to the few experimental data on the hydrodynamics of these beds.[16,17] Accordingly, the design and scaling-up of conical fluidized beds is not straightforward, given that bed geometry, the ratio of inlet diameter to bed height and operating conditions highly influence gas–solid flow regime. Furthermore, hydrodynamic parameters such as pressure drop, solid volume fraction, and velocity significantly affect the performance of the conical bed. Optimizing the performance of conical fluidized beds requires a thorough understanding of the mixing characteristics and interactions between the gas and solid phases. The standard noninvasive measurement techniques used for the determination of particle trajectories and velocities are as follows: pitot tube,[18] Laser-Doppler anemometry,[19] video technique,[20] radioactive particle tracking,[21] and particle image velocimetry.[22] Nevertheless, techniques based on an optical-fiber probe are also promising for this purpose.[23–29]

In recent years, with the development of high performance computers, researchers have used numerical methods to study the flow behavior of fluidized beds.[30–35] Computational fluid dynamic (CFD) modeling helps to explain the details of gas-fluidized bed hydrodynamics and allows developing quantitative process models that enable predictive scaling-up and process optimization. However, experimental data are required for evaluating the accuracy of CFD simulation.

Although the Eulerian–Eulerian multiphase model with the kinetic theory of granular flow (KTGF) has been widely used as an essential constitutive model for simulating gas–solid flow, the role of wall boundary condition (BC) is critical to the accuracy of CFD models. The BC represents the energy flux into the granular medium at the walls. As granular energy is produced at the wall, the granular temperature increases, with the solids being pushed toward the interior. Several BCs have been proposed in the literature for the continuum gas–solid flow models. Thus, Benyahia et al.[36–38] have used three different wall BCs in their simulations, which are those recommended by Johnson and Jackson[39] and by Jenkins,[40] and free-slip for particle velocity with a specified granular temperature of zero. Johnson and Jackson's BC uses a specularity coefficient φ to describe the roughness of

Correspondence concerning this article should be addressed to A. Bahramian at bahramian@aut.ac.ir.

the wall. A value of zero for φ represents perfectly specular (smooth) collisions (free-slip BC), whereas a value of unity represents perfectly diffuse (rough) collisions (no-slip BC).[36,38] Jenkins' BC accounts for two limits of low and high friction depending on whether the particles are assumed to slide (low friction) or bounce back tangentially (high friction) when colliding with the walls. Benyahia and coworkers investigated the limits of low friction/free-slip and high friction/no-slip BC for the solid phase at the wall of a riser.[36] Their results show that a no-slip BC causes unrealistically large granular energy production at the wall. However, their results better predict the solid volume fraction near the riser wall, with the value of the friction coefficient being small. Taghipour et al.[41] and Almuttahar and Taghipour[42] applied the BCs developed by Johnson and Jackson[39] to the simulation of a circulating fluidized bed riser. They reported that the choice of free- or no-slip BC affects the behavior predicted for FCC catalyst particles near the riser wall. Recently, Bahramian et al.[43] and Bahramian and Olazar[44,45] used an Eulerian–Eulerian two-phase model with different drag models and various wall BCs. The model was used to analyze the dynamic pressure and bed expansion ratio of conical fluidized beds. Their study shows that the Gidaspow drag model with a partial-slip BC agrees reasonably well with the experimental data for dynamic pressure, and the same drag model with a free-slip BC can better predict the bed expansion ratio.

Several alternatives for determining the slip velocity between gas and particle velocities are described in the literature.[41,46–49] One approach is to assume that solid slip velocity is equal to particle terminal velocity. This assumption is often inaccurate, particularly for fine particles. Certain researchers have suggested modified versions of this assumption that include the influence of vessel orientation, static bed heights, and the particle's physical properties.[4,13,16,32,50] Alternatively, slip velocity is estimated either experimentally or numerically from the difference between gas and solid particle velocities.[48,49] Finally, a third approach is to inject a few labeled tracer particles and measure their velocities experimentally.[48]

The main objective here is to develop a CFD model for describing the hydrodynamics of a conical fluidized bed. Accordingly, the optical fiber technique is used as a first step to provide a set of experimental data for axial solid velocity in different sections of a bench-scale conical fluidized bed containing polydispersed dried TiO_2 particles. In addition, the open-source CFD code-MFIX is used to simulate the radial profiles of axial solid velocities in the bed at different air velocities and for different static bed heights. The radial profiles of gas velocity and slip velocity have been determined numerically from the difference between simulated gas and solid particle velocities. The performance of the Eulerian–Eulerian two-phase model with the KTGF and three wall BCs for the particulate phase, corresponding to no-slip, partial-slip, and free-slip case, is evaluated by comparing its predictions with our experimental results. The solid particle behavior near the wall is studied in detail by comparing the effect of the different wall BCs. Moreover, a grid-sensitivity analysis has been carried out using uniform and near-wall refinement schemes to ensure that numerical results are close to the experimental data. The drag models suggested by Syamlal and O'Brien,[51] Ahmadi and Ma,[52–54] Arastoopour et al.,[55] and Gidaspow[56] have been used in the simulation and their suitability has been examined.

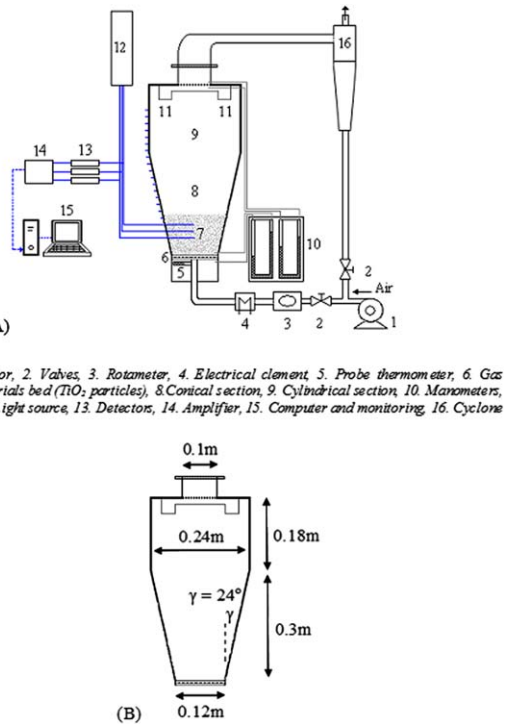

1. Air compressor, 2. Valves, 3. Rotameter, 4. Electrical clement, 5. Probe thermometer, 6. Gas distributor, 7. Materials bed (TiO_2 particles), 8.Conical section, 9. Cylindrical section, 10. Manometers, 11. Bagfilters, 12. Light source, 13. Detectors, 14. Amplifier, 15. Computer and monitoring, 16. Cyclone

Figure 1. (A) Schematic diagram of the experimental apparatus.

(B) Dimensions of the bed. [Color figure can be viewed in the online issue, which is available at wileyonlinelibrary.com.]

Experimental Setup

The experiments have been performed in a commercially available transparent Plexiglas conical fluidized bed (STREA-1 from Aeromatic, Switzerland). This transparent vessel allowed visual observation of particle motion, and it is geometrically similar to the industrial-scale units used in the pharmaceutical, petrochemical, and food industries. A schematic diagram and the dimensions of the experimental apparatus are shown in Figure 1 (Figures 1A,B, respectively). The setup contains a gas distributor plate that is covered with a stainless steel wire mesh (Standard Mesh No. 200) at the bottom of the bed. Air at 60°C and atmospheric pressure is supplied to the bed by an air compressor.

The particles used throughout this experiment are dried TiO_2 microparticles in the 90–600 μm range, belonging to the B/D boundary of Geldart's classification. The TiO_2 particle size distribution is as follows: 2% smaller than 90 μm, 4% in the 90–125 μm range, 16% in the 125–200 μm range, 32% in the 200–300 μm range, 26% in the 300–400 μm range, and 20% in the 400–600 μm range. The mean particle diameter of the mixture is 280 μm.

Four different static bed heights, H_0, corresponding to 0.012, 0.024, 0.048, and 0.060 m, are analyzed in this work. The experiments have been performed by increasing air velocity, U_a, from the fixed bed state to fully fluidized state at a superficial air velocity of 1.4 m/s and then decreasing the flow rate until zero velocity (initial state) is reached.

An optical-fiber probe technique is used to measure the mean solid velocities in the spout and annular regions and at

the interface between these zones. A stepper motor controller is used to change the position of the probe at the selected axial positions, z. When a particle passes near the head of the probe, it reflects light emitted by the central fiber. An Nd-YAG solid-state laser is used as a light source with a frequency of 50 Hz. A 12-V light source transmits light to the emitting fiber and a filter controls the intensity of the beam. The light signal is collected by photodiodes and converted into voltage (1–100 mV). The signals then pass through the amplifier (−12 to +12 V). An analog/digital interface sends the reflected light data to the computer for processing. Solid velocities are calculated based on a statistical analysis using the cross-correlation function incorporated into a MATLAB program. Additional details of the fiber-optic technique are described in previous articles.[26,27,43–45]

CFD Modeling and Simulation Procedure

The fundamental equations for mass and momentum conservation in each phase are summarized in Appendix A. Although the actual flow is not fully isothermal, the energy conservation equation is not considered and isothermal flow is assumed. The granular temperature equation, which originates from the KTGF, is also solved to account for the conservation of fluctuation energy in the solid phase. However, the equations for momentum and granular temperature need to be closed by providing appropriate constitutive equations for the granular stress tensor, granular energy fluxes, and rate of energy exchange. Equations (B1–B11) listed in Appendix B are the constitutive equations for granular stress tensor, shear viscosity, solid pressure, collisional dissipation energy, and other parameters, which are required for the closure of both the solid phase momentum equation and the granular temperature equation. The gas–solid momentum exchange coefficient is assumed to include only the drag contribution. Four different drag models are used here, which are those proposed by Syamlal and O'Brien,[51] Ahmadi and Ma,[52–54] Arastoopour et al.,[55] and Gidaspow[56] (Appendix C).

Assumptions and BCs

The assumptions and the BCs used in the simulations are:

1. Continuous phase is treated as ideal gas.
2. The axisymmetric BC is applied along the axis of symmetry.
3. The velocities and volume fractions in the inlet of both phases are specified. The air inlet velocity is assumed to be uniform in the radial direction and the values of 0.1, 0.3, 0.7, and 1.4 m/s are used, whereas the inlet solid velocity is set to zero.
4. Outflow BCs with zero velocity gradients at the outlet for each phase along the axial direction are assumed. Furthermore, the pressure at the outlet is assumed to be atmospheric.
5. The no-slip BC at the wall is used for the gas phase, whereas the BC equations developed by Johnson and Jackson[39] are applied to the tangential velocity of the solid phase. These equations are described in Appendix D (Table D1). Three types of slip conditions corresponding to no-slip, partial-slip, and free-slip BCs are set out in Appendix D for the solid phase. The specularity coefficient is used to determine the slip condition of the solid phase at the wall (Table D2 in Appendix D). This parameter accounts for the fraction of collisions that transfer momentum to the wall. The value of the specularity coefficient varies from zero (free-slip condition) to one (no-slip condition).

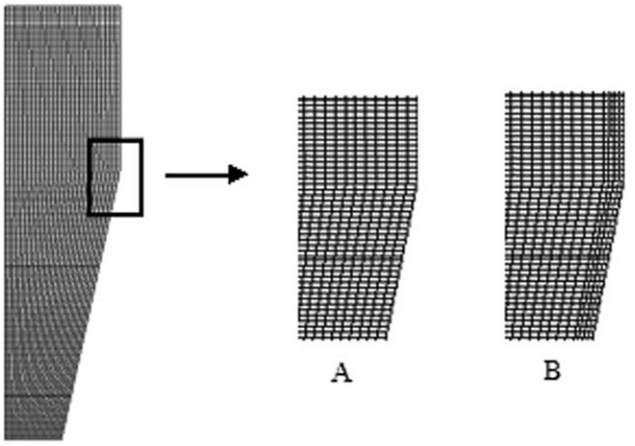

Figure 2. Computational grid used in the simulations.

(A) Uniform scheme, (B) near wall refinement ($r/R = 0.4$–0.5) [the number of grid cells in both schemes is 46,000].

Numerical procedure

The Eulerian–Eulerian two-phase model with the KTGF and the k-epsilon turbulence model have been solved by the finite volume technique for both the solid and gas phases to simulate hydrodynamic behavior in a conical fluidized bed. The open source software MFIX code is used for solving the governing equations (http://mfix.netl.doe.gov). The two-dimensional (2-D) axisymmetric segregated solver is chosen in all simulations. The pressure-velocity coupling is analyzed by using the phase coupled SIMPLEC algorithm.

A first-order upwind scheme and implicit formulation have been used to discretize the convection term. The time step for unsteady simulations was varied from 5×10^{-5} to 1×10^{-3} s, depending on the solution convergence. The properties of TiO_2 particles are used in the simulation to compare the simulated results with experimental data. Particles are assumed to be perfectly spherical and monosized; thus, only one solid phase with an average particle size of 280 μm is considered. The computation time for simulating 5.5 s of real time was approximately 22 h on a PC with a 3.2-GHz Pentium 4.

Grid-sensitivity Analysis

Grid-sensitivity analysis is essential to ensure CFD simulation is independent of the grid size.[36,57,58] This concept has meaning only when convergence criteria are clearly defined. Grid independency is checked in this study to ensure that accurate numerical results are obtained. The computational domains are discretized using 11,500, 23,000, 34,500, and 46,000 grid cells with a rectangular structure. Therefore, grid sizes are around 2.2 mm in the axial direction and in the 1.8–2.6 mm range in the radial direction, depending on the uniform scheme or near-wall model approach. A typical computational mesh obtained using 46,000 cells is shown in Figure 2. The simulation performed in the conical bed with a uniform scheme is shown in Figure 2A. Furthermore, near-wall refinement is used for fine-tuning grid size in the 0.4–0.5 r/R range, Figure 2B. This mesh is selected to fulfill the conditions for the use of the near-wall model and achieve a solution that is independent of mesh density.

Results and Discussion

Experimental results

Experimental analysis was performed on a bed containing polydispersed dried TiO_2 particles. On increasing air velocity, the bed gradually changes from a fixed condition to a fully fluidized state. At first, the fine particles are suspended in the airflow and, by increasing airflow velocity, they finally become fluidized, whereas the large agglomerate particles do not reach fluidization. Bed volume also expands gradually by increasing airflow velocity until large heavy agglomerates start to move and a transition regime from the channeling regime to full fluidization regime is reached in the bed.[2,3,31,55,56,59] However, large agglomerates of the particle phase are observed in certain cases at the bottom of the conical bed. It should be noted that the fluidization of fine particles and/or large agglomerates is delayed and even completely stopped due to the presence of interparticle cohesive forces and/or weight.[10,30,60–62] The bed containing polydispersed particles fluidizes faster, given that the large particles act as local turbulence promoters, whereas the fine particles slide down, behaving as if in a boiling state. In this bed, the fine particles form a layer around the relatively large agglomerate particles and play a lubricating role, which lowers the apparent viscosity, promotes bed fluidization and increases air–solid mixing. Experimental operation shows that a small amount of ultrafine TiO_2 particles with a diameter less than 2 μm leaves the bed. Bag filters are placed at the top of the bed to prevent particles larger than 2 μm leaving the vessel at high airflow velocities.

A vigorous particle motion is observed at high airflow velocities and the entire bed is fluidized (axial and radial solid circulation), with a turbulent flow regime, especially for low particle loadings. Visual observations reveal that fine TiO_2 particles travel faster than large agglomerates, and the concentration of large agglomerates is lower in the center of the column than near the wall. Furthermore, although most of the particles are moving quickly in the bed, a low percentage of larger TiO_2 particles and particle agglomerates move relatively slowly near the bottom section. Accordingly, although the simulation of turbulent flow regimes has been approached in the literature,[15,30,32,37,42,55,63] the modeling of the flow in a conical fluidized bed with low particle loadings requires appropriate turbulence models and drag functions in order to predict experimental trends.

The solid particles follow a circulation pattern according to the so-called gulf-effect. Thus, the particles descending toward the intermediate section of the vessel following positions near the wall accelerate as they approach the bottom of the vessel, with their maximum velocity being attained at the core and in a region near the spout zone (approximate range: $-0.05 \leq r/R \leq 0.05$).

The turbulent fluctuation in the axial direction (z) is much larger than in the other two directions because the gas is fed into the system in this direction. Therefore, the axial solid velocity profiles measured in the conical fluidized bed at different bed levels for various airflow rates are shown in Figures 3, 5, and 6. All the experiments show that axial solid velocity decreases with the dimensionless radial distance, from a maximum near the axis to a negative value at the wall, which is evidence of a downward particle motion near the wall. These figures correspond to different bed particle loadings and, in all cases, the maximum axial solid velocity is found in the spout-annular zone (approximate range: $0.08 \leq r/R \leq 0.12$). Accordingly, the experimental data will be compared with the simulation results in order to validate the more suitable turbulence model.

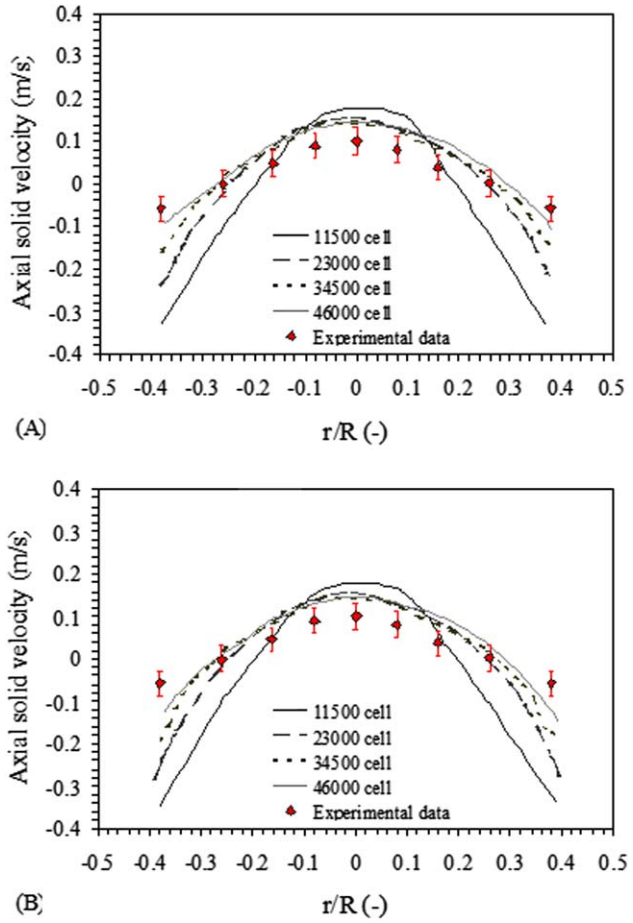

Figure 3. Comparison of experimental axial solid velocity profiles with simulation results obtained using the Gidaspow drag model with 11,500, 23,000, 34,500, and 46,000 grid cells.

(A) Uniform scheme, (B) near-wall model [$z = 0.2$ m, $H_0 = 0.048$ m, and $U_a = 0.3$ m/s]. [Color figure can be viewed in the online issue, which is available at wileyonlinelibrary.com.]

Simulation results

A series of 2-D computer simulations have been performed for the laboratory scale conical fluidized bed using MFIX code. Special attention has been paid to the effect of different drag models, that is, those by Syamlal and O'Brien,[51] Ahmadi and Ma,[52–54] Arastoopour et al.,[55] and Gidaspow.[56]

Figure 3 compares the experimental data for the axial solid velocity profile with the simulation results obtained using the Gidaspow drag model with 11,500, 23,000, 34,500, and 46,000 grid cells. Figures 3A,B show the simulation results for these cells when a uniform scheme and near-wall model, respectively, are considered. These results have been obtained at $z = 0.2$ m for an initial bed height of 0.048 m and at an inlet gas velocity of 0.3 m/s.

As observed, the simulation results obtained with 11,500, 23,000, and 34,500 grid cells deviate from the experimental data. In particular, the axial solid velocity records high negative values near the wall, whereas the results obtained with

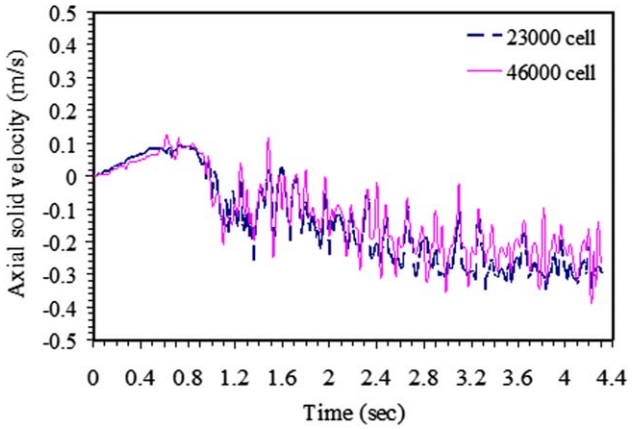

Figure 4. Temporal variation of simulated solid velocity near the bed wall for 23,000 and 46,000 grid cells [$z = 0.2$ m, $H_0 = 0.048$ m, and $U_a = 0.3$ m/s].

[Color figure can be viewed in the online issue, which is available at wileyonlinelibrary.com.]

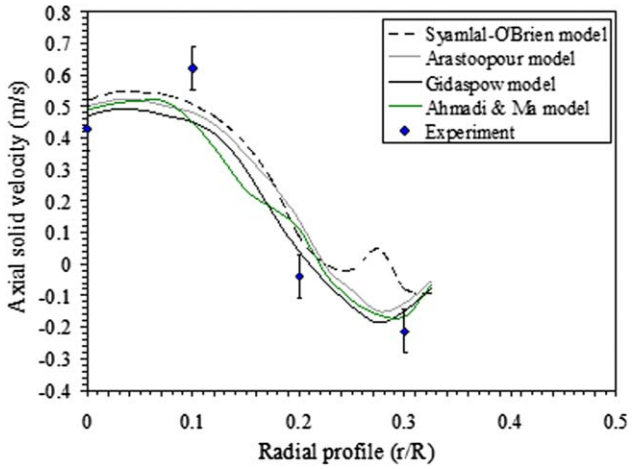

Figure 5. Comparison of 2-D simulation results with the experimental data at $z = 0.1$ m for $H_0 = 0.048$ m and $U_a = 0.7$ m/s.

[Color figure can be viewed in the online issue, which is available at wileyonlinelibrary.com.]

46,000 grid cells are in reasonable agreement with the experimental data. It should be noted that the size of a cell in a computational mesh using 46,000 cells is around 10 times the mixture's mean particle diameter. This is consistent with other studies of grid-sensitivity analysis.[36,38,57,58,64] A comparison of Figures 3A,B shows that the results of numerical simulation with and without wall refinement are similar, although there is a slight difference in the wall. Therefore, a grid size of 46,000 cells with near-wall model approach is selected in the numerical simulations to assess the sensitivity of different drag models.

Figure 4 shows the temporal variation in the simulated solid velocity near the bed wall at $H_0 = 0.048$ m and $U_a = 0.3$ m/s. The probe is located at $r/R = 0.38$, and $z = 0.2$ m, where the solid particles fall along the wall in the conical section. These results have been obtained using the Gidaspow[56] drag model with 23,000 and 46,000 grid cells. As observed, the simulated solid velocity obtained using the finer mesh of 46,000 cells gives way to a signal with higher fluctuations than when using a mesh of 23,000 cells. Furthermore, after a simulation time of around 3.0 s, the axial solid velocities near the wall fluctuate between mean values of -0.25 and -0.22 m/s when using meshes of 23,000 and 46,000 cells, respectively. It should be noted that particle flow is downward near the wall due to the weight force and low upward gas velocity in this zone. In fact, the gas bypasses the particles in the dense annular region, but raises them through the central core to the bed surface, where they fall back onto the annular zone, thereby producing continuous particle circulation and mixing. Furthermore, Figure 4 shows the particles are transported upward (positive solid velocity) at the start of the fluidization due to gas bubbles passing through the whole bed.

In order to give the reader more insight into the fully fluidized state over the periodic time of 4.3 s, we have created an animation file of solid volume fraction (dilute and dense flow regimes are depicted in blue and red, respectively), which is available in the Supporting Information File. The simulation time of 4.3 s used in the file is sufficient to obtain results independent of the averaging time. Nevertheless, a simulation time of 5.5 s was selected in the numerical simulations to ensure a fully fluidized state.

Figure 5 shows the results predicted for axial solid velocity using the free-slip BC. They have been obtained at $z = 0.1$ m for a 2-D bed of $H_0 = 0.048$ m and $U_a = 0.7$ m/s. In agreement with the experimental data, the simulation results show that the axial solid velocity decreases with the dimensionless radial distance from a maximum value near the axis to negative values indicating a downward particle motion near the wall. As observed in Figure 5, all four drag models lead to roughly similar results, although Syamlal–O'Brien[51] model records an increase near the wall that is not realistic.

An error analysis provides the following values for the different drag models: 23% for Syamlal–O'Brien,[51] 9% for Gidaspow,[56] 15% for Arastoopour et al.,[55] and 11% for Ahmadi–and Ma.[52–54] The Syamlal–O'Brien[51] model predicts more consistent results at the spout-annulus interface ($0.08 \le r/R \le 0.12$), whereas those by Gidaspow[56] and Ahmadi and Ma[52–54] provide a better fit for the experimental results near the wall. In a previous article,[44] we found that the optimum values for the restitution coefficient, e_{ss}, are those corresponding to particle–particle friction and maximum particle packing values of 0.9 and 0.67, respectively.

The axial solid velocity along the wall is more sensitive to the specularity coefficient, which inevitably affects solid back-mixing and, therefore, the conical fluidized bed performance. Figures 6 and 7 compare the experimental data with those obtained by simulating the axial solid velocity profiles, using three types of wall BCs, namely, no-slip, partial-slip, and free-slip. The wall BC represents the frictional contact between particles and wall boundaries (particle-wall friction). These profiles correspond to a level of $z = 0.05$ m, an initial bed height of 0.048 m and air velocities of 0.7 and 1.4 m/s. The simulation results for the Gidaspow drag model are shown in Figure 6, and for Ahmadi–Ma model in Figure 7. Both models record roughly similar results for the different slip BCs. The trend of both the experimental data and the simulation results is fairly similar, that is, the axial solid velocity increases slightly to a peak value in the spout-annular zone and then decreases as the radial distance is higher. Furthermore, the simulation results follow a similar trend at the spout-annular interface for all the BCs.

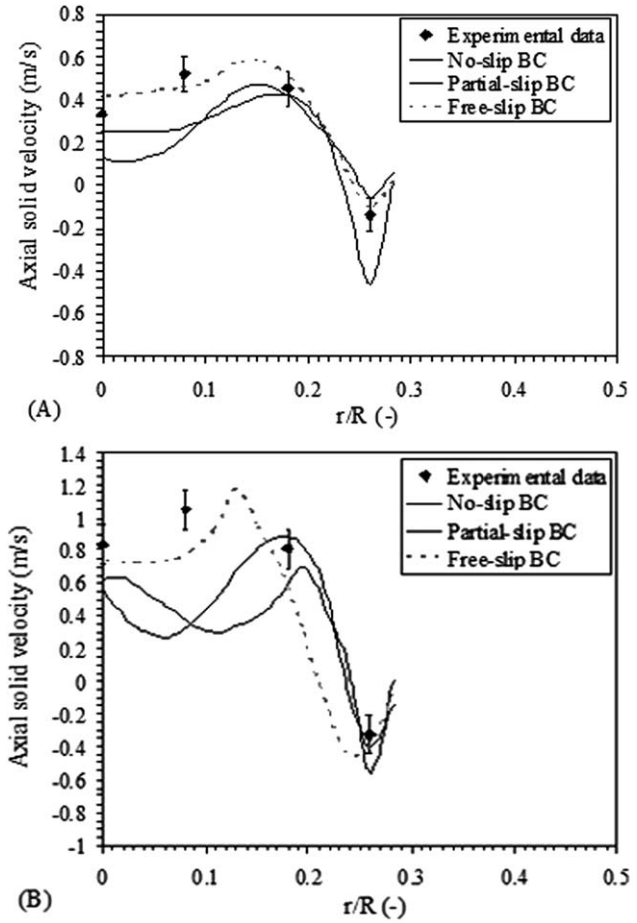

Figure 6. Experimental data and simulated radial profiles of the axial solid velocity using Gidaspow drag model $z = 0.05$ m, (A) $U_a = 0.7$ m/s, (B) $U_a = 1.4$ m/s.

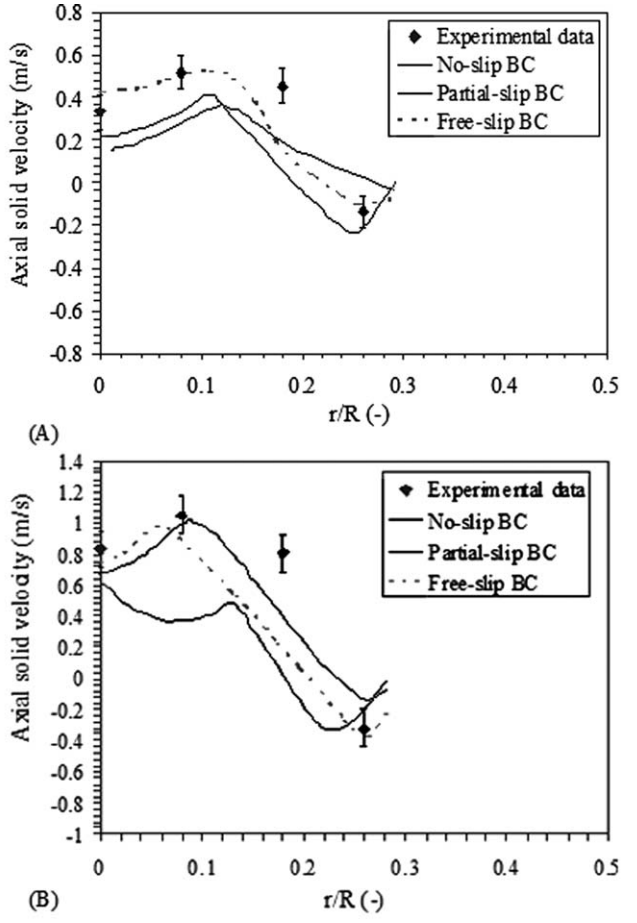

Figure 7. Experimental data and simulated radial profiles of the axial solid velocity using Ahmadi–Ma drag model $z = 0.05$ m, (A) $U_a = 0.7$ m/s, (B) $U_a = 1.4$ m/s.

Nevertheless, considerable deviations are observed, especially for the no-slip and partial-slip BCs at a high air velocity corresponding to Figures 6B and 7B. When the free-slip wall BC ($\varphi = 0$) is used, there is no friction between particles and wall, which means more particles flowing downward, thus resulting in higher particle velocity and so a high solid volume fraction at the bottom of the conical fluidized bed. When the no-slip wall BC ($\varphi = 1$) is used, there is major friction between particles and wall, and the dissipation caused by particle-wall collisions hinders the downward flow of particles, thus resulting in a low simulated particle velocity near the wall.

The results obtained for the conical fluidized bed differ from those obtained by Olazar et al.[27] for conical spouted beds, given that the maximum upward axial velocity in the latter is measured at the axis of bed, whereas this value in conical fluidized beds is located in the spout zone near the spout-annular interface.[65,66] This trend is related to the trajectories of the larger particles in the spout, which in conical spouted beds follow mainly positions near the spout-annulus interface,[67] whereas in conical fluidized beds they rise near the axis. Accordingly, axial solid velocity decreases due to gravity and the dissipation of energy caused by frictional contacts between particles.

Table 1 shows the relative error between the experimental data and the simulation results of axial solid velocity obtained by the Gidaspow[56] and Ahmadi and Ma[52–54] drag models. In view of these errors, the following observations are made: (1) The simulation results obtained by Ahmadi

Table 1. Relative Errors of Axial Solid Velocity Obtained by Using Different BCs

		Relative Error (%)					
		No-Slip BC		Partial-Slip BC		Free-Slip BC	
U_a (m/s)	Drag Model	Spout Zone	Other Zones	Spout Zone	Other Zones	Spout Zone	Other Zones
0.7	Gidaspow	19.5	15.0	22.0	10.7	9.5	7.0
	Ahmadi-Ma	15.5	13.0	21.0	11.0	11.7	8.6
1.4	Gidaspow	25.6	14.0	24.3	13.3	10.4	6.0
	Ahmadi-Ma	18.2	10.0	15.0	11.8	12.6	9.0

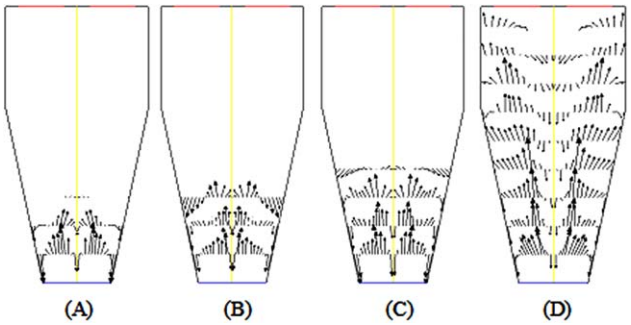

Figure 8. Vector plot of solid velocity applying no-slip BC [(A) 0.1 m/s, (B) 0.3 m/s, (C) 0.7 m/s, (D) 1.4 m/s].

[Color figure can be viewed in the online issue, which is available at wileyonlinelibrary.com.]

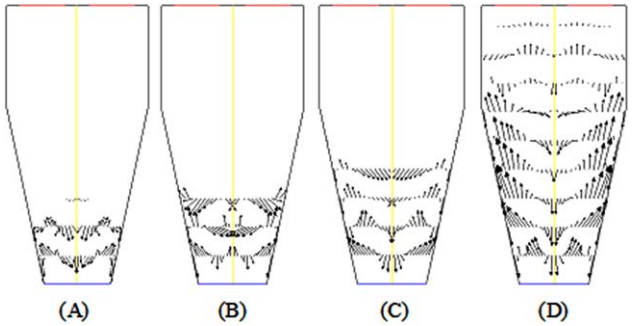

Figure 9. Vector plot of solid velocity applying partial-slip BC [(A) 0.1 m/s, (B) 0.3, (C) 0.7 m/s, (D) 1.4 m/s].

[Color figure can be viewed in the online issue, which is available at wileyonlinelibrary.com.]

and Ma[52–54] drag model with no-slip and partial-slip BCs are more consistent with the experimental data than those obtained by the Gidaspow[56] drag model. However, the latter provides slightly more consistent results when the free-slip BC is used. The explanation lies in the higher solid volume fraction simulated for lower particle-wall friction and/or no-friction. (2) The axial solid velocity profiles obtained using the free-slip BC is more consistent for both drag models. This suggests that a low value of particle-wall friction should be used in the model for conical fluidized beds with smooth walls. (3) The highest deviations between experimental data and simulation results are found at the spout zone (approximate range: $r/R \leq 0.07$). This suggests there is higher energy dissipation in the spout zone due to particle–particle contacts.

Figures 8–10 show the local solid velocity vectors at different axial positions in the bed for air velocities of 0.1, 0.3, 0.7, and 1.4 m/s. The data correspond to $H_0 = 0.060$ m, $e_{ss} = 0.9$, and the Gidaspow drag model. As observed, airflow velocity significantly affects solid flow patterns. Thus, Figures 8 and 10 corresponding to no-slip and free-slip BCs, respectively, show that the upward axial velocity in the spout zone peaks near the bed axis. Axial velocity decreases as the radial position is higher, being close to zero at the spout-annulus interface. In the annular zone, (approximate range $r/R \geq 0.28$), the downward velocity peaks at the wall. Although these are the main trends, the simulated results also predict a slight downward motion at the axis of the contactor.

The simulated vector profiles obtained for a partial-slip BC are shown in Figure 9, and they are different from those obtained with the other BCs (Figures 8 and 10). Thus, particle descent is observed almost exclusively at the center of the bed, with ascent at the wall. Nevertheless, visual observations in the experiments reveal that particles move upward in the central region and downward near the wall. Thus, the vector profiles predicted by using no-slip or free-slip BCs are more consistent with visual observations.

The simulation data predict vigorous particle circulation in conical fluidized beds with low particle loadings. The magnitude of the vectors indicates that, overall, solid velocity is high at the center and intermediate radial positions in this system, although the no-slip BC predicts a slight descending trend around the axis for high airflow velocities. Figures 8D and 10D, corresponding to high velocities, show a solid circulation pattern with particles ascending near the axis and descending near the wall. This pattern is predicted especially by using the free-slip BC, Figure 10D, and has been observed in conical fluidized beds, risers, and spouted beds. Furthermore, the free-slip wall BC gives way to higher particle velocities than the no-slip wall BC–either downward at the wall or upward in the spout zone. Thus, wall friction causes the velocity near the wall to be lower than in the central region, and particles circulate toward the bottom of the vessel, so maximum downward velocity is attained near the bed wall at the bottom.[17,27,31,34,63] The vector plot of particle velocity with the free-slip wall BC (Figure 10) records a higher particle circulation rate, thus enhancing solid backmixing along the wall.

Figures 11–13 show the distribution of the instantaneous contour plot of the solid velocity for the air velocities of 0.1, 0.3, 0.7, and 1.4 m/s and static bed heights of 0.012, 0.048, and 0.060 m. These simulations are obtained by using the Gidaspow[56] drag model with free-slip BCs. These velocity distributions correspond to 4.0 s after the airflow is first introduced into the bed. As observed, increasing air velocity leads to different solid flow patterns. Figures 11A–13A, corresponding to an air velocity lower than the minimum fluidization velocity, U_{mf}, show there are channels near the center of the bed with air passing through the bed. At the highest static bed height of 0.060 m, this model predicts large bubbles in the bed, Figure 13A. The values predicted

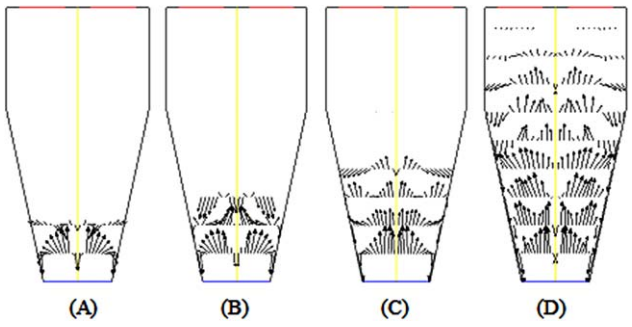

Figure 10. Vector plot of solid velocity applying free-slip BC [(A) 0.1 m/s, (B) 0.3, (C) 0.7 m/s, (D) 1.4 m/s].

[Color figure can be viewed in the online issue, which is available at wileyonlinelibrary.com.]

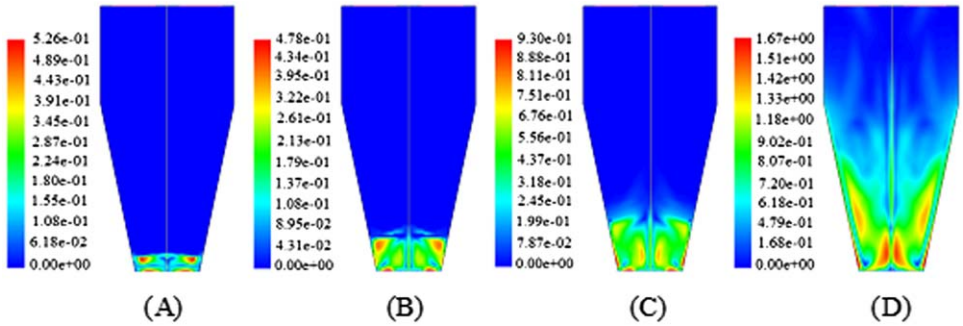

Figure 11. Instantaneous contour plot of the solid velocity applying free-slip BC [(A) 0.1, (B) 0.3, (C) 0.7, (D) 1.4 m/s] $H_0 = 0.012$ m.

[Color figure can be viewed in the online issue, which is available at wileyonlinelibrary.com.]

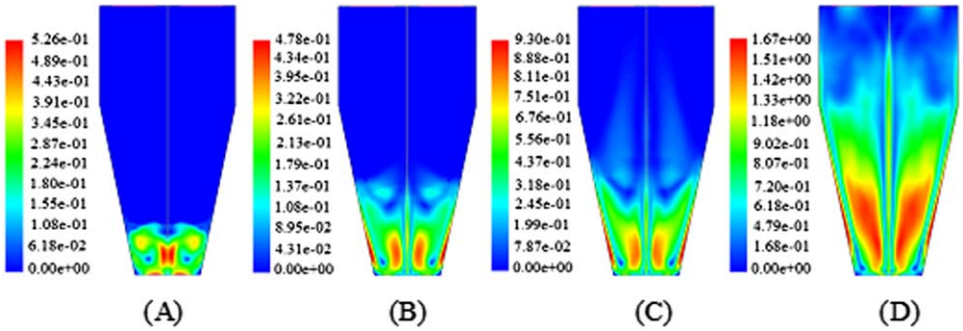

Figure 12. Instantaneous contour plot of the solid velocity applying free-slip BC [(A) 0.1, (B) 0.3, (C) 0.7, (D) 1.4 m/s] $H_0 = 0.048$ m.

[Color figure can be viewed in the online issue, which is available at wileyonlinelibrary.com.]

for the minimum fluidization velocity at the static bed heights of 0.012, 0.048, and 0.060 m are 0.102, 0.117, and 0.236 m/s, respectively. Figures 11B–13B show the results for $U_a = 0.3$ m/s, which is higher than the minimum fluidization velocity. In this case, the bed gradually expands, channels are disrupted, and fluidization occurs at the central region of the bed. When the airflow velocity is further increased, the height of the expanded bed increases (Figure 11C–13C). For higher air velocities, Figures 11D–13D show that the air simply blows through the bed without forming a spout and annular zones, and complete fluidization state occurs.

The flow patterns of solid particles at high air velocities in conical fluidized beds are different from those in spouted beds. In the latter, the air initially passes through the packed bed forming a channel that grows in height as air velocity is increased. When air velocity reaches the minimum spouting velocity, U_{ms}, the channel reaches the upper surface of the bed and forms a fountain, which is typical of spouted beds. The formation of the spout in the center and in the annulus near the walls is also observed.[23,65,68] The spout and annular zones are not defined in conical fluidized beds, and a vigorous particle motion is observed at high airflow velocities, as shown in Figures 12D–13D.

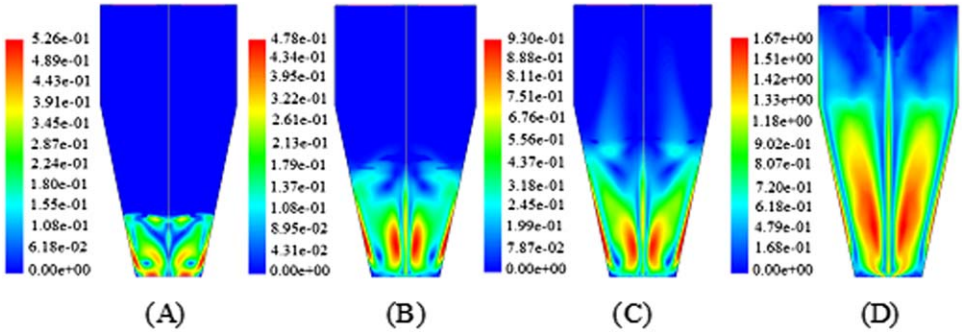

Figure 13. Instantaneous contour plot of the solid velocity applying free-slip BC [(A) 0.1, (B) 0.3, (C) 0.7, (D) 1.4 m/s] $H_0 = 0.060$ m.

[Color figure can be viewed in the online issue, which is available at wileyonlinelibrary.com.]

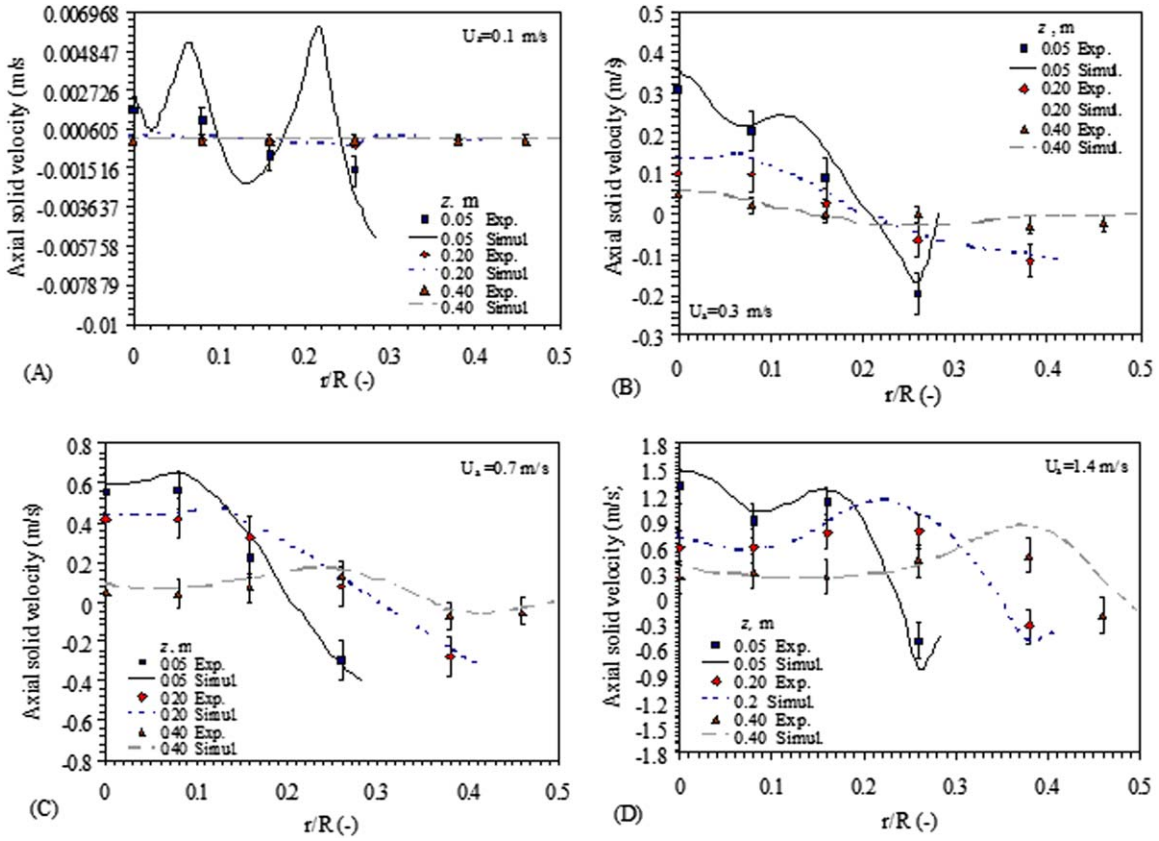

Figure 14. Dimensionless radial profile of axial solid velocity for $H_0 = 0.012$ m.

[Color figure can be viewed in the online issue, which is available at wileyonlinelibrary.com.]

As observed in Figures 11–13, there is good particle circulation when the static bed height is increased from 0.012 to 0.048 and to 0.060 m, with the expanded bed height being consistent with the experimental data. Furthermore, low bed channeling is predicted for the lowest static bed height, corresponding to 0.012 m, which evidences that, in addition to air velocity, static bed height is an essential parameter for estimating particle flow patterns.

The effect of static bed height on the profiles of axial mean solid velocity computed using the Gidaspow[56] drag model and with a free-slip BC is shown in Figures 14–16 for different air inlet velocities. As observed, although the simulated results are slightly higher than the experimental data, the overall model predictions are reasonable. The deviation may be due to the consideration of mono-sized particles in the simulation, whereas the actual TiO_2 particles have a wide particle-size distribution, that is, particles with different size and shape travel at different velocities in the bed.

Figures 14–16 clearly show that air velocity has a significant effect on particle velocity in the spout zone but little effect on particle velocity in the annular zone. This differs from the results obtained by He et al.[23–25] for spouted beds. They found that particle velocity in the annular zone of spouted beds increases as air inlet velocity is increased. The differences between spouted and conical beds probably arise from the fact that particle velocity in the annular zone of conical fluidized beds is relatively low compared to spouted beds and, consequently, the variation in particle velocity with air inlet velocity is relatively small in conical beds. Solid velocities in both the spout and the annular zones decrease as the radial distance from the center of the bed is higher and the velocity profiles in the two zones become flatter until zero velocity is recorded at the top of the fountain, and the particles then fall onto the annular zone. These results are qualitatively similar to those obtained by Goldschmidt et al.,[15] Kmiec,[16] Olazar et al.,[8,26,27] and Huilin et al.[68] for conical–cylindrical spouted beds and jet-spouted beds.

As static bed height is increased from 0.012 m (Figure 14) to 0.024 m (Figure 15) and then to 0.048 m (Figure 16), once the spout has been formed the air in all cases passes preferentially through this central bed zone. As observed, the mean axial solid velocities at the bottom (at $z = 0.05$ m) for a high air velocity (Figures 14D–16D) are different for the three static bed heights studied, 0.012, 0.024, and 0.048 m. Visual observations reveal that high static bed heights cause particle agglomeration. This is because larger particle flow is not fully developed in the bottom section. When the flow of air and solid particles is fully developed and reaches a steady state, there is no acceleration or deceleration of particles and, therefore, no changes in solid velocity and friction.

The dimensionless radial profile of axial solid velocity reveals that velocity values near the wall are negative, especially in the bottom section, and its magnitude decreases as bed height is increased. Furthermore, particle entrainment occurs for average superficial air velocities lower than the terminal velocity of the particles. This is explained by the fact that, for a fully developed flow, the local velocities in the spout zone are higher than the average superficial air velocity.[16,24]

Figure 14B shows that low particle loadings with low air velocities give way to a wave-like structure due to air

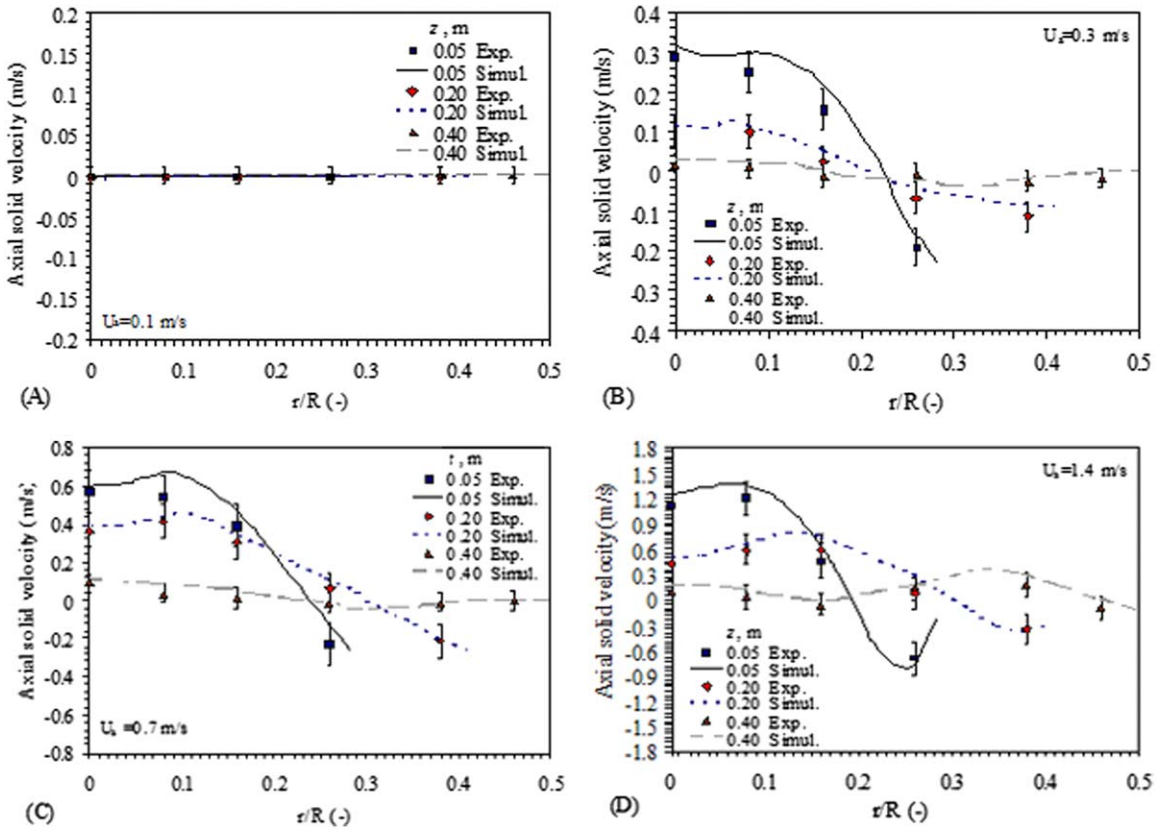

Figure 15. Dimensionless radial profile of axial solid velocity for $H_0 = 0.024$ m.

[Color figure can be viewed in the online issue, which is available at wileyonlinelibrary.com.]

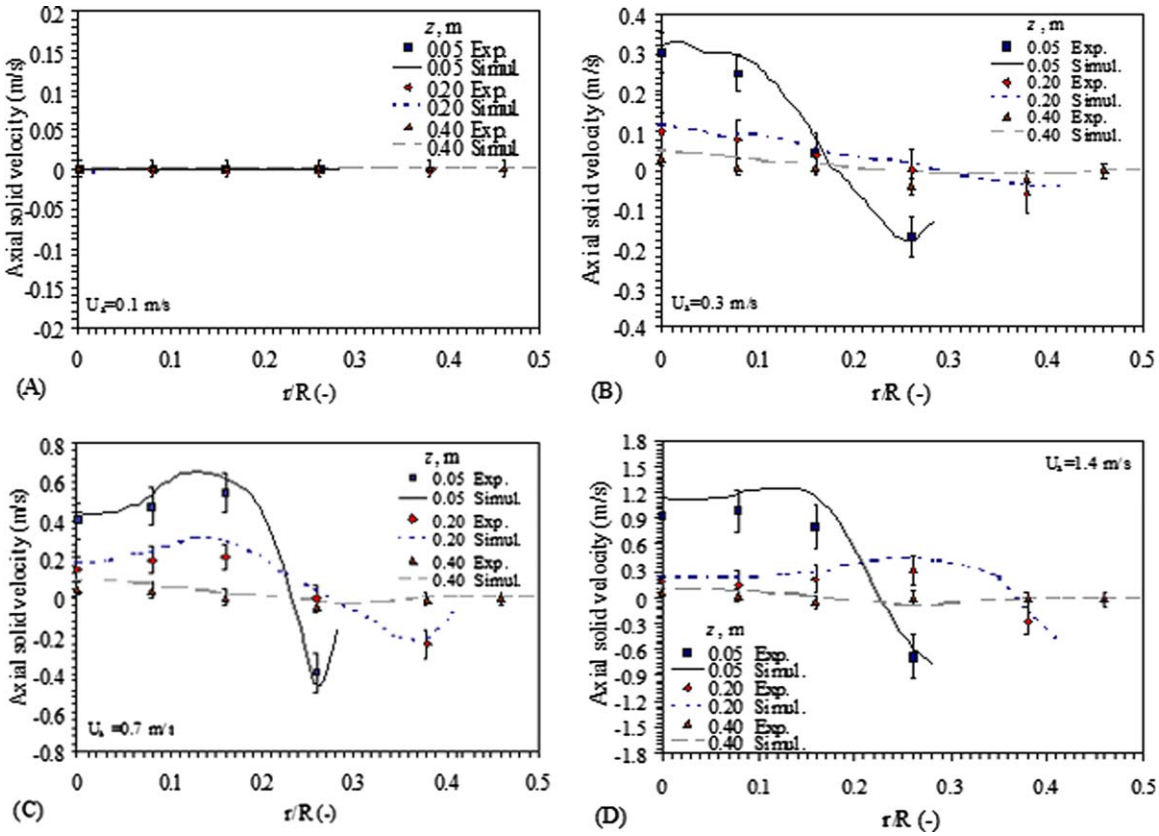

Figure 16. Dimensionless radial profile of axial solid velocity for $H_0 = 0.048$ m.

[Color figure can be viewed in the online issue, which is available at wileyonlinelibrary.com.]

Table 2. Relative Error Between the Experimental Data and Simulation Results of Axial Solid Velocity

	Relative Error (%)		
Air Velocity (m/s)	0.012 (m)	0.024 (m)	0.048 (m)
0.1	5.11	2.04	2.01
0.3	5.87	6.52	7.74
0.7	6.37	7.21	7.61
1.4	6.88	7.54	8.93

bubbles traveling from the bottom to the top, whereas high air velocities (Figures 14C,D) give way to a negligible drag force and complete solid circulation.

At relatively high particle loadings (Figures 16A–D), major flow resistance is caused by the solid particles themselves and the friction at their interface, because the air flow gives them upward acceleration, and bed behavior is close to a spouted bed, especially at low air velocity (Figure 16B).

Table 2 shows the relative error between the experimental data and the simulation results of axial solid velocity obtained by the Gidaspow[56] drag model. The highest deviations between experimental and simulation results are found at the highest particle loading, $H_0 = 0.048$ m, which is explained by higher TiO_2 particle loadings causing more particle agglomeration and changes in local solid velocities in the bed. Thus, as static bed height is increased by 100% (from 0.012 to 0.024 m) and 300% (from 0.012 to 0.048 m) at an air velocity of 0.7 m/s, the relative error increases by 13 and 19%, respectively.

Figure 17 shows the dimensionless radial profiles of axial air velocity obtained for different bed heights at air inlet velocities of 0.7 and 1.4 m/s by using a free-slip BC and the Gidaspow[56] drag model. Air velocities peak in the central bed zone and then gradually decrease toward the wall, where they drop to almost zero. Therefore, most of the airflow passes through the central bed zone.

The dimensionless radial profiles of local slip velocity are shown in Figure 18. As observed, slip velocity is minimum in the central region, where air and particles flow cocurrently, and then gradually increases along the radial direction with slip velocity peaking near the wall, where air and particles flow countercurrently. Figures 18A,B also show that particle slip velocity increases for TiO_2 particles when air velocity is increased. Thus, an increase in air velocity has two effects on slip velocity, a positive one due to a lower particle velocity per se and a negative one due to the lower particle velocity caused by counter flow velocity.

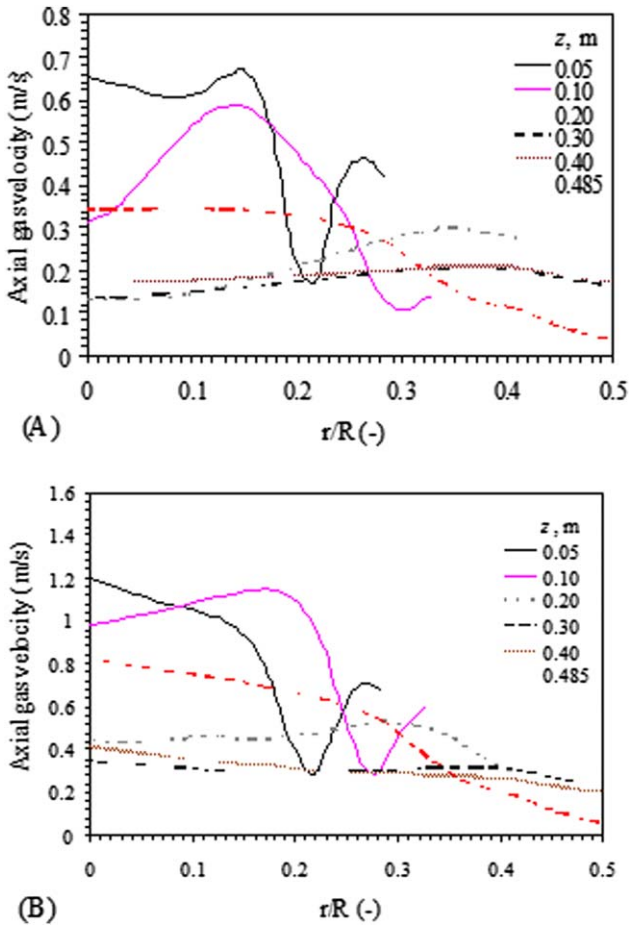

Figure 17. Evolution of axial air velocity profiles with dimensionless radial distance for $H_0 = 0.048$ m [(A) $U_a = 0.7$ m/s, (B) $U_a = 1.4$ m/s].

[Color figure can be viewed in the online issue, which is available at wileyonlinelibrary.com.]

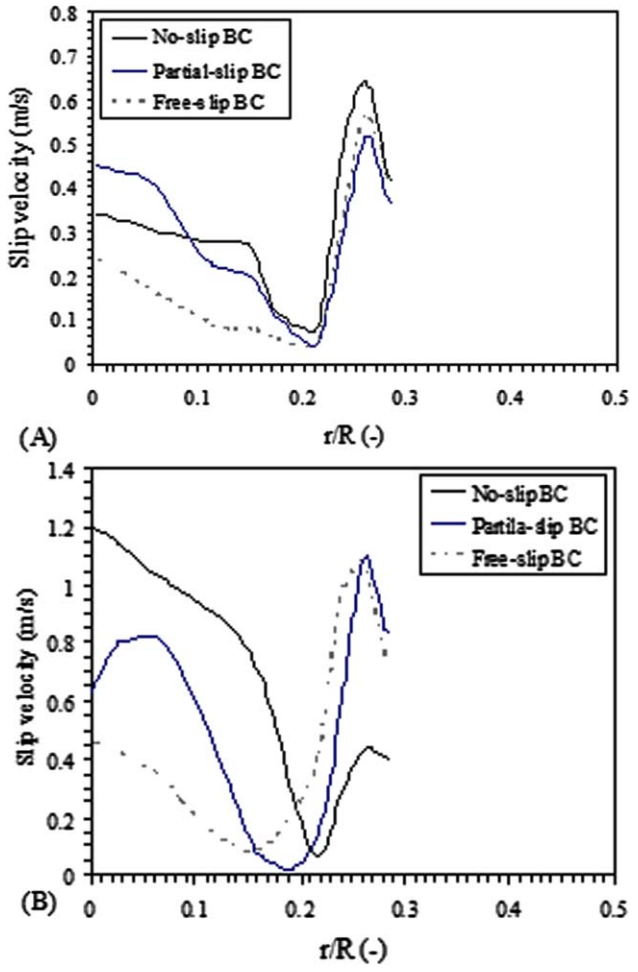

Figure 18. Dimensionless radial profile of slip velocity for $H_0 = 0.048$ m [(A) $U_a = 0.7$ m/s, (B) $U_a = 1.4$ m/s].

[Color figure can be viewed in the online issue, which is available at wileyonlinelibrary.com.]

Conclusions

The hydrodynamic behavior of polydispersed dried TiO_2 particles with a mean diameter of 280 μm belonging to the B/D boundary of Geldart's classification has been studied experimentally and numerically in a conical fluidized bed at different superficial air velocities. The effect of different static bed heights on the radial profiles of axial solid velocity has been experimentally determined with an optical fiber technique. A suitable numerical method based on the finite volume method has been used to discretize the continuity, momentum, and granular temperature equations for solid and gas phases. The Eulerian–Eulerian two-phase model involving the KTGF and a k-epsilon turbulent model with three wall BCs (no-slip, partial-slip, and free-slip) have been used for the solid phase in the numerical simulations. The methodology used in the numerical simulations of each type of BC has been validated by comparing it with experimental data. The number of grid cells required for ensuring a grid-independent solution is determined using two schemes, namely, uniform and near-wall refinement models. A cell size of around 10 times the mean particle diameter of the mixture is selected in the numerical simulations with the near-wall model approach to assess the sensitivity of different drag models.

More simulations have been run using the Arastoopour,[55] Syamlal–O'Brien,[51] Ahmadi–Ma,[52–54] and Gidaspow[56] drag functions. The main conclusion is that the drag functions proposed by Gidaspow[56] and Ahmadi and Ma[52–54] give a better prediction than the other drag functions posited by Syamlal and O'Brien[51] and Arastoopour et al.[55] for predicting the axial solid velocity. However, all the simulated values of axial solid velocity are slightly lower than that experimentally measured at the air velocities investigated. The dimensionless radial profile of axial solid velocity reveals that its values near the wall are negative, especially in the bottom section, and its magnitude decreases with increasing bed height. The overall results show that the free-slip BC provides a slightly better prediction of axial solid velocity and lower error at the different static bed heights studied. This evidences that the free-slip wall BC without particle-wall collisions should be used in the conical fluidized bed with very smooth walls. Slip velocity is minimum in the central region, where there is cocurrent flow of air and particles, and then gradually increases along the radial direction to a maximum near the wall, where there is countercurrent flow of air and particles. The experimental and simulated results show that low particle loadings with low air velocity ($U_a = 0.1$ m/s) give way to a wave-like structure in the bed due to air bubbles travelling from the bottom of the bed to the top, whereas full solid circulation is obtained at high air velocities ($U_a \geq 0.7$ m/s). The highest deviations between experimental data and simulation results are found in the spout zone, whereas the simulation results in the other zones are more consistent with the experimental data. Furthermore, large errors between experimental and simulation results are also found at high initial static bed heights ($H_0 \geq 0.048$ m), given that an increase in TiO_2 particle loading causes greater particle agglomeration and changes in axial solid velocity in the bed. Therefore, in addition to air velocity, the initial static bed height is also an essential parameter for estimating particle flow patterns in the design and scaling-up of conical fluidized beds.

Acknowledgment

The authors would like to thank the Hamedan University of Technology and Laser and Optic Research School of Iran for optical experiments and digital treatment.

Notation

Symbols

B = slip coefficient, dimensionless
Bo_g = granular bond number, dimensionless
C_D = drag coefficient, dimensionless
d_i = inlet diameter, m
d_p = particle diameter, m
$d_{p,avg}$ = average particle diameter, m
e_{ss} = restitution coefficient, dimensionless
$\boldsymbol{g}$ = acceleration due to gravity, m s^{-2}
$g_{0,ss}$ = radial distribution coefficient, dimensionless
h = total column height, m
H = expanded bed height, m
H_0 = static bed height, m
$\bar{\bar{I}}$ = stress tensor, dimensionless
I_{2D} = second invariant of the deviatoric stress tensor, dimensionless
k = turbulent kinetic energy, kg m^{-1} s^{-3}
$k\theta_s$ = diffusion coefficient for granular energy, kg m^{-1} s^{-1}
MFIX = Multiphase Flow with Interphase eXchanges
P = pressure, Pa
p_f = frictional stress, dimensionless
R,r = radius, m
Re = Reynolds number, dimensionless
t = time, s
U,u = gas velocity, m s^{-1}
v = particle velocity, m s^{-1}
x = weight fraction
z = axial direction

Greek letters

α_i = loose bed volume fraction, dimensionless
β = interphase momentum exchange coefficient, dimensionless
$\gamma\theta_m$ = collisional dissipation of energy, kg.m^{-1} s^{-3}
γ = cone angle
θ_i = granular temperature, m^2 s^{-2}
λ_i = bulk viscosity, kg m^{-1} s^{-1}
μ_i = shear viscosity, kg m^{-1} s^{-1}
ν_i = kinematic viscosity, m^2 s^{-1}
ρ_i = density, kg m^{-3}
$\bar{\tau}_i$ = stress tensor, Pa
ϕ_{gs} = transfer rate of kinetic energy, kg m^{-1} s^{-3}
φ = specularity coefficient, dimensionless

Subscripts

a = air
b = bulk
g = gas
i = general index
mf = minimum fluidization
o = outlet
p = particle
q = phase
s = solid
t = terminal (e.g., v_t is the terminal velocity)
w = wall

Literature Cited

1. Pugsley T, Chaplin G, Khanna P. Application of measurement techniques to conical lab-scale fluidized bed dryers containing pharmaceutical. *Trans IChemE*. 2007;85:273–283.
2. Wormsbecker M, Adams A, Pugsley T, Winter C. Segregation by size difference in a conical fluidized bed of pharmaceutical granulate. *Powder Technol*. 2005;153:72–80.
3. Tanfara H, Pugsley T, Winters C. Effect of particle size distribution on local voidage in a bench-scale conical fluidized bed dryer. *Drying Technol*. 2002;20:1273–1289.

4. Kunii D, Levenspiel O. Design for physical systems. In: Brenner H, editor, Fluidization Engineering, 2nd ed. Boston: Butterworth-Heinemann, 1991.
5. Senadeera W, Wijesinghe B, Young G, Bhandari B. Fluidization characteristics of moist food particles. *Int J Food Eng*. 2006;2:1–13.
6. Leckner B, Szentannai P, Winter F. Scale-up of fluidized-bed combustion–a review. *Fuel*. 2011;90:2951–2964.
7. Adanez J, Gayan P, Celaya J, de Diego LF, Garcia-Labiano F, Abad A. Chemical looping combustion in a 10 kWth prototype using a CuO/Al_2O_3 oxygen carrier: effect of operating conditions on methane combustion. *Ind Eng Chem Res*. 2006;45:6075–6080.
8. Olazar M, San Jose MJ, Zabala G, Bilbao J. A new reactor in jet spouted bed regime for catalytic polymerizations. *Chem Eng Sci*. 1994;49:4579–4588.
9. Olazar M, Aguado R, Bilbao J, Barona A. Pyrolysis of sawdust in a conical spouted bed contactor with a HZSM-5 catalyst. *AIChE J*. 2000;46:1025–1033.
10. Geldart D. The effect of particle size and size distribution on the behavior of gas-fluidized beds. *Powder Technol*. 1972;6:201–215.
11. Geldart D. Types of gas fluidization. *Powder Technol*. 1973;7:285–292.
12. Syamlal M, O'Brien TJ. Fluid dynamic simulation of O_3 decomposition in a bubbling fluidized bed. *AIChE J*. 2003;49:2793–2801.
13. Depypere F, Pieters JG, Dewettinck K. Expanded bed height determination in a fluidized bed reactor. *J Food Eng*. 2009;67:353–359.
14. Duarte CR, Olazar M, Murata VV, Barrozo MAS. Numerical simulation and experimental study of fluid-particle flows in a spouted bed. *Powder Technol*. 2008;188:195–205.
15. Goldschmidt MJV, Kuipers JAM, van Swaaij WPN. Hydrodynamic modeling of dense gas-fluidized beds using the kinetic theory of granular flow: effect of coefficient of restitution on bed hydrodynamics. *Chem Eng Sci*. 2001;72:561–568.
16. Kmiec A. Hydrodynamics of flow and heat transfer in spouted beds. *Chem Eng J*. 1980;19:189–200.
17. Sau DC, Mohanty S, Biswal KC. Critical fluidization velocities and maximum bed pressure drops of homogeneous binary mixture of irregular particles in gas–solid tapered fluidized beds. *Powder Technol*. 2008;186:241–246.
18. Johnsson F, Larsson G, Leckner B. Pressure and flow fluctuations in a fluidized bed-interaction with the air-feed system. *Chem Eng Sci*. 2002;57:1379–1392.
19. Müller CR, Hartung G, Hult J, Dennis JS, Kaminski CF. Laser diagnostic investigation of the bubble eruption patterns in the freeboard of fluidized beds: simultaneous acetone PLIF and stereoscopic PIV measurements. *AIChE J*. 2009;55:1369–1382.
20. Barletta D, Russo P, Poletto M. Dynamic response of a vibrated fluidized bed of fine and cohesive powders. *Powder Technol*. 2013;237:276–285.
21. Khanna P, Pugsley T, Tanfara H, Dumont H. Radioactive particle tracking in a lab-scale conical fluidized bed dryer containing pharmaceutical granule. *Can J Chem Eng*. 2008;86:563–570.
22. Agarwal G, Lattimer B, Ekkad S, Vandsburger U. Experimental study on solid circulation in a multiple jet fluidized bed. *AIChE J*. 2012;58:3003–3015.
23. He YL, Qin SZ, Lim CJ, Grace JR, Zhu JX. Measurements of voidage profiles in a spouted beds. *Can J Chem Eng*. 1994;72:229–234.
24. He YL, Qin SZ, Lim CJ, Grace JR. Particle velocity profiles and solid flow patterns in spouted beds. *Can J Chem Eng*. 1994;72:561–568.
25. He YL, Lim CJ, Grace JJR, Qin S. Spout diameters in full and half spouted beds. *Can J Chem Eng*. 1998;76:702–706.
26. Olazar M, San Jose MJ, Lamosas R, Alvarez S, Bilbao J. Study of local properties in conical spouted beds using an optical fiber probe. *Ind Eng Chem Res*. 1995;34:4033–4039.
27. Olazar M, San Jose MJ, Izquierdo MA, Ortiz de Salazar A, Bilbao J. Effect of operating conditions on solid velocity in the spout, annulus and fountain of spouted beds. *Chem Eng Sci*. 2001;56:3585–3594.
28. Qin SZ, Liu G. Application of optical fibers to measurement and display of fluidized systems. *Fluid Sci Technol*. 1982;47:258–267.
29. Liu J, Grace JR, Bi X. Novel multifunctional optical-fiber probe II. *AIChE J*. 2003;49:1421–1432.
30. Rhodes MJ, Wang XS, Nguyen M, Stewart P, Liffman K. Onset of cohesive behavior in gas fluidized beds: a numerical study using DEM simulation. *Chem Eng Sci*. 2001;56:4433–4438.
31. McKeen T, Pugsley T. Simulation and experimental validation of a freely bubbling bed of FCC catalyst. *Powder Technol*. 2003;129:139–152.
32. Li J, Kuipers JAM. Gas-particle interactions in a dense gas-fluidized beds. *Chem Eng Sci*. 2003;58:711–718.
33. Hosseini SH, Ahmadi G, Rahimi R, Zivdar M, Nasr Esfahany M. CFD studies of solids hold-up distribution and circulation patterns in gas–solid fluidized beds. *Powder Technol*. 2010;200:202–215.
34. Neri A, Gidaspow D. Riser hydrodynamics: simulation using kinetic theory. *AIChE J*. 2000;46:52–67.
35. Guo Y, Wu CY, Thornton C. Modeling gas-particle two-phase flows with complex and moving boundaries using DEM-CFD with an immersed boundary method. *AIChE J*. 2013;4:1075–1087.
36. Benyahia S, Syamlal M, O'Brien TJ. Study of the ability of multiphase continuum models to predict core-annulus flow. *AIChE J*. 2007;53:2549–2568.
37. Benyahia S, Syamlal M, O'Brien TJ. Evaluation of boundary conditions used to model dilute turbulent gas/solids flows in a pipe. *Powder Technol*. 2005;156:62–72.
38. Li T, Benyahia S. Evaluation of wall boundary condition parameters for gas-solids fluidized-bed simulations. *AIChE J*, in press. Article first published online: May 16, 2013.
39. Johnson PC, Jackson R. Frictional-collisional constitutive relations for granular materials, with application to plane shearing. *J Fluid Mech*. 1987;176:67–93.
40. Jenkins JT. Boundary conditions for rapid granular flow: flat, frictional walls. *Trans ASME*. 1992;59:120–127.
41. Taghipour F, Ellis N, Wong C. Experimental and computational study of gas-solid fluidized bed hydrodynamics. *Chem Eng Sci*. 2005;60:6857–6867.
42. Almuttahar A, Taghipour F. Computational fluid dynamics of high density circulating fluidized bed riser: study of modeling parameters. *Powder Technol*. 2008;185:11–23.
43. Bahramian A, Ostadi H, Olazar M. Evaluation of drag models for predicting the fluidization behavior of silver oxide nanoparticle agglomerates in a fluidized bed. *Ind. Eng. Chem. Res*. 2013;52:7569–7578.
44. Bahramian A, Olazar M. Fluidization of micronic particles in a conical fluidized bed: experimental and numerical study of static bed height effect. *AIChE J*. 2012;58:730–744.
45. Bahramian A, Olazar M. Profiling solid volume fraction in a conical bed of dry micrometric particles: measurements and numerical implementations. *Powder Technol*. 2011;212:181–192.
46. Yang YL, Jin LY, Yu ZQ, Wang ZW. Investigation on slip velocity distributions in the riser of dilute circulating fluidized bed. *Powder Technol*. 1992;73:67–73.
47. Wang J, van der Hoef MA, Kuipers JAM. CFD study of the minimum bubbling velocity of Geldart A particles in gas-fluidized beds. *Chem Eng Sci*. 2010;65:3772–3785.
48. Tallon S, Davies CE, Barry B. Slip velocity and axial dispersion measurements in a gas-solid pipeline using particle tracer analysis. *Powder Technol*. 1998;99:125–131.
49. Yang YL, Jin Y, Yu ZQ, Zhu JX, Bi HT. Local slip behaviors in the circulating fluidized bed. *AIChE Symp Ser*. 1993;81:296.
50. Abrahamsen AR, Geldart D. Behavior of gas-fluidized beds of fine powders. *Part I: homogeneous expansion. Powder Technol*. 1980;26:35–46.
51. Syamlal M, O'Brien TJ. Computer simulation of bubbles in a fluidized bed. *AIChE Symp Ser*. 1989;85:22–31.
52. Ahmadi G, Ma D. A kinetic model for granular flows of nearly elastic particles in grain-inertia regime. *Int J Bulk Solid Storage Silos*. 1986;2:8–16.
53. Ahmadi G, Ma D. A thermodynamic formulation for dispersed multiphase turbulent flows I. Basic theory. *Int J Multiphase Flow*. 1990;16:323–340.
54. Ahmadi G. Thermodynamics of multi temperature fluids with applications to turbulence modeling. *Appl Math Model*. 1985;9:271–274.
55. Arastoopour H, Pakdel P, Adewumi M. Hydrodynamics analysis of dilute gas-solid flow in a vertical pipe. *Powder Technol*. 1990;62:163–170.
56. Gidaspow D. *Multiphase Flow and Fluidization*, *1st ed*. London: Academic press, 1994.
57. Cloete S, Amini S, Johansen ST. A fine resolution parametric study on the numerical simulation of gas–solid flows in a periodic riser section. *Powder Technol*. 2011;205:103–111.
58. Kriebitzsch SHL, van der Hoef MA, Kuipers JAM. Fully resolved simulation of a gas-fluidized bed: a critical test of DEM models. *Chem Eng Sci*. 2013;91:1–4.

59. Ogawa S, Umemura A, Oshima N. On the equations of fully fluidized granular materials. *J Appl Math Phys*. 1980;31:483–493.
60. Hristov J. Magnetically assisted gas–solid fluidization in a tapered vessel: Part I. *Magnetization-LAST mode*. *Particuology*. 2009;7:26–34.
61. Wang XS, Rahman F, Rhodes M. Nanoparticle fluidization and Geldart's classification. *Chem Eng Sci*. 2007;62:3455–3461.
62. Huang Q, Zhang H, Zhu J. Onset of an innovative gasless fluidized bed comparative study on the fluidization of fine powders in a rotating drum and a traditional fluidized bed. *Chem Eng Sci*. 2010;65:1261–1273.
63. Cao J, Ahmadi G. Gas-particle two-phase turbulent flow in a vertical duct. *Int J Multiphase Flow*. 1995;21:1203–1228.
64. Sundaresan S, Eaton J, Koch D, Ottino JM. Appendix 2: report of study group on disperse flow. *Int J Multiphase Flow*. 2003;29:1069–1087.
65. San Jose MJ, Olazar M, Alvarez S, Morales A, Bilbao J. Local porosity in conical spouted beds consisting of solids of varying density. *Chem Eng Sci*. 2005;60:2017–2025.
66. Luo KB, Liu W, Zhu JX, Beeckmans JM. Characterization of gas upward–solids downward countercurrent fluidized flow. *Powder Technol*. 2001;115:36–44.
67. San José MJ, Olazar M, Peñas FJ, Bilbao J. Segregation in conical spouted beds with binary and tertiary mixtures of equidensity spherical particles. *Ind Eng Chem Res*. 1994;33:1838–1844.
68. Huilin L, Yurong H, Wentie L, Ding J, Gidaspow D, Bouillard J. Computer simulations of gas-solid flow in spouted bed using kinetic-frictional stress model of granular flow. *Chem Eng Sci*. 2004;59:865–878.
69. Gibilaro LG, Di Felice R, Waldram SP. Generalized friction factor and drag coefficient correlations for fluid-particle interactions. *Chem Eng Sci*. 1985;40:1817–1823.
70. Ergun S. Fluid flow through packed columns. *Chem Eng Prog*. 1952;48:89–94.
71. Wen CY, Yu YH. A generalized method for predicting minimum fluidization velocity. *AIChE J*. 1966;12:610–612.
72. Lu HL, He YR, Gidaspow D, Yang LD. Size segregation of binary mixture of solids in bubbling fluidized beds. *Powder Technol*. 2003;134:86–97.

Appendix A

The conservation laws used in the present study are summarized in Table A1

Table A1. Governing Equation for Gas/Solid Flows

Mass conservation for phase i (i = g for gas and i = s for solid)

$$\frac{\partial}{\partial t}(\alpha_i.\rho_i)+\nabla.(\alpha_i.\rho_i.\vec{\mathbf{v}}_i)=0 \tag{A1}$$

Linear momentum balance for gas and solid phases

$$\frac{\partial}{\partial t}\left(\alpha_{\mathrm{g}}.\rho_{\mathrm{g}}.\vec{\mathrm{U}}_{\mathrm{g}}\right)+\nabla.\left(\alpha_{\mathrm{g}}.\rho_{\mathrm{g}}.\vec{\mathrm{U}}_{\mathrm{g}}\cdot\vec{\mathrm{U}}_{\mathrm{g}}\right)=-\alpha_{\mathrm{g}}\nabla P+\nabla.\overline{\overline{\tau_{\mathrm{g}}}}-\beta\left(\vec{\mathrm{U}}_{\mathrm{g}}-\vec{\mathbf{v}}_{\mathrm{s}}\right)+\alpha_{\mathrm{g}}.\rho_{\mathrm{g}}.\vec{\mathbf{g}} \tag{A2}$$

$$\frac{\partial}{\partial t}(\alpha_{\mathrm{s}}.\rho_{\mathrm{s}}.\vec{\mathbf{v}}_{\mathrm{s}})+\nabla.(\alpha_{\mathrm{s}}.\rho_{\mathrm{s}}.\vec{\mathbf{v}}_{\mathrm{s}}.\vec{\mathbf{v}}_{\mathrm{s}})=-\alpha_{\mathrm{s}}\nabla P+\nabla.\overline{\overline{\tau_{\mathrm{s}}}}-\nabla P_{\mathrm{s}}+\beta\left(\vec{\mathbf{U}}_{\mathrm{g}}-\vec{\mathbf{v}}_{\mathrm{s}}\right)+\alpha_{\mathrm{s}}.\rho_{\mathrm{s}}.\vec{\mathbf{g}} \tag{A3}$$

Transport equation for the solid phase granular temperature

$$\frac{3}{2}\left[\frac{\partial}{\partial t}(\alpha_{\mathrm{s}}.\rho_{s}.\theta_{s})+\nabla.(\alpha_{\mathrm{s}}.\rho_{\mathrm{s}}.\vec{\mathbf{v}}_{\mathrm{s}}.\theta_{\mathrm{s}})\right]=(-P_{\mathrm{s}}\bar{\bar{\mathrm{I}}}+\overline{\overline{\tau_{\mathrm{s}}}}):\nabla.\vec{\mathbf{v}}_{\mathrm{s}}-\nabla.(\mathrm{k}_{\theta}.\nabla.\theta_{\mathrm{s}})-\gamma_{\theta}+\phi_{\mathrm{gs}} \tag{A4}$$

Appendix B

Constitutive equations are listed in Table B1.

Table B1. Constitutive Equations of Gas/Solid Flow

Solid stress tensor

$$\bar{\bar{\tau}}_{\mathrm{s}}=\mu_{\mathrm{s}}\left(\nabla\vec{\mathbf{v}}_{\mathrm{s}}+(\nabla\vec{\mathbf{v}}_{\mathrm{s}})^{T}\right)+\left(\lambda_{\mathrm{s}}-\frac{2}{3}\mu_{\mathrm{s}}\right)\nabla.\vec{\mathbf{v}}_{\mathrm{s}} \tag{B1}$$

where solid shear viscosity is

$$\mu_{s}=\mu_{s,col}+\mu_{s,kin}+\mu_{s,fr} \tag{B2}$$

TABLE B1. *Continued*

and the collisional contribution to shear viscosity is[39]

$$\mu_{s,col} = \frac{4}{5}\alpha_s.\rho_s.g_{0,ss}(1+e_{ss})\sqrt{\frac{\theta_s}{\pi}} \tag{B3}$$

The kinetic contribution to shear viscosity[68]

$$\mu_{s,kin} = \frac{10\rho_s.d_s\sqrt{\theta_s.\pi}}{96\alpha_s(1+e_{ss})g_{0,ss}}\left[1+\frac{4}{5}g_{0,ss}.\alpha_s(1+e_{ss})\right]^2 \tag{B4}$$

The frictional contribution to shear viscosity[56]

$$\mu_{s,fr} = p_f \sin(\varphi)/2\sqrt{I_{2D}} \tag{B5}$$

Solid phase bulk viscosity[68]

$$\lambda_s = \frac{4}{3}\alpha_s^2.\rho_s.d_s.g_{0,ss}(1+e_{ss})\sqrt{\frac{\theta_s}{\pi}} \tag{B6}$$

Collision dissipation energy

$$\gamma_\theta = \frac{12(1-e_{ss}^2)g_{0,ss}}{d_s\sqrt{\pi}}\rho_s.\alpha_s^2.\theta_s^{3/2} \tag{B7}$$

Solid pressure

$$P_s = \alpha_s.\rho_s.\theta_s + 2\rho_s(1+e_{ss})\alpha_s^2.g_{0,ss}.\theta_s \tag{B8}$$

Thermal energy diffusion coefficient[56]

$$k_\theta = \frac{25\rho_s.d_s\sqrt{\theta_s.\pi}}{64(1+e_{ss}).g_{0,ss}}.\left[1+\frac{6}{5}.\alpha_s.g_{0,ss}.(1+e_{ss})\right]^2 + 2\rho_s.\alpha_s^2.d_s(1+e_{ss})g_{0,ss}\sqrt{\frac{\theta_s}{\pi}} \tag{B9}$$

Radial distribution function[69,70]

$$g_{0,ss} = \left[1-\left(\frac{\alpha_s}{\alpha_{s,max}}\right)^{1/3}\right]^{-1} \tag{B10}$$

Dissipation of granular temperature by gas damping

$$\phi_{gs} = -3\beta.\theta_s \tag{B11}$$

Appendix C

The drag models and the corresponding correlations for β used in this study are summarized in Table C1.

Table C1. Drag Models Used in this Study

Syamlal and O'Brien (1988)

Syamlal and O'Brien[12,51] proposed a drag coefficient model based on measuring the particle terminal velocity in fluidized beds

$$\beta = \frac{3}{4}\frac{\alpha_s.\alpha_g.\rho_g}{v_{r,s}^2.d_s}C_D.\left(\frac{\mathrm{Re}_s}{v_{r,s}}\right).|\vec{\mathbf{v}}_s - \vec{\mathbf{U}}_g| \tag{C1}$$

where the Reynolds number based on relative velocity is defined as

$$\mathrm{Re}_s = \frac{\rho_g.d_s.|\vec{\mathbf{v}}_s - \vec{\mathbf{u}}_g|}{\mu_g} \tag{C2}$$

$\mathbf{v}_{r,s}$ is the terminal velocity correlation for the solid phase

$$\boldsymbol{v}_{r,s}=0.5\left(A-0.06\mathrm{Re}_s+\sqrt{(0.06\mathrm{Re}_s)^2+0.12\mathrm{Re}_s(2B-A)+A^2}\right) \tag{C3}$$

with

$$A=\alpha_g^{4.14} \tag{C4}$$

and

$$B=P\alpha_g^{1.28}\alpha_g \le 0.85 \tag{C5}$$

$$B=\alpha_g^{Q}\alpha_g \rangle 0.85 \tag{C6}$$

where P and Q are parameters based on the minimum fluidization velocity.

Drag coefficient

$$C_D=\left(0.63+\frac{4.8}{\sqrt{\mathrm{Re}_s/v_{r,s}}}\right)^2 \tag{C7}$$

Arastoopour et al. (1990)

Arastoopour et al.[55] modified the pressure drop correlation proposed by Gibilaro et al.[69] and suggested a gas–solid drag coefficient model expressed as

$$\beta=\left[\frac{17.3}{\mathrm{Re}_s}+0.336\right].\frac{\rho_s.\alpha_s.\alpha_g^{-2.8}}{d_s}.|\vec{v}_s-\vec{U}_g| \tag{C8}$$

Ahmadi and Ma (1990)

Ahmadi and Ma[52–54] suggested a thermodynamically consistent formulation

$$\beta=\frac{18\mu_g v^{\alpha}}{d_s^2}.\frac{\left[1+0.1(\mathrm{Re}_s)^{0.75}\right]}{\left(1-\frac{v^{\alpha}}{v_m^{\alpha}}\right)^{2.5v_m^{\alpha}}} \tag{C9}$$

Here, v_m^{α} is the limiting dense packing volume fraction for shear flows. For a single size spherical particulate phase, $v_m = 0.64356$.

Gidaspow (1994)

Gidaspow[56] model combines the Ergun[70] equation for dense flows

$$\beta_{\mathrm{Eurgun}}=150\frac{\alpha_s^2\mu_g}{\alpha_g d_s^2}+1.75\frac{\alpha_s\rho_g}{d_s}|\vec{\mathbf{v}}_s-\vec{\mathbf{U}}_g|\alpha_g \le 0.8 \tag{C10}$$

with the formulation by Wen and Yu[71] for dilute flows

$$\beta=\frac{3}{4}C_D\frac{\alpha_s\alpha_g\rho_g|\vec{\mathrm{v}}_s-\vec{\mathrm{U}}_g|}{d_s}.\alpha_g^{-2.65} \qquad \alpha_g \rangle 0.8 \tag{C11}$$

The drag coefficient is given by

$$C_D=\frac{24}{\mathrm{Re}_s}\left[1+0.15(\alpha_g.\mathrm{Re}_s)^{0.687}\right] \qquad \mathrm{Re}_s \langle 1000 \tag{C12}$$

$$C_D=0.44 \qquad \mathrm{Re}_s \ge 1000 \tag{C13}$$

Lu and Gidaspow[72] introduced a transition function, which gives a rapid continuous transition from one regime to the other. This function is given by

$$\varphi_{gs}=\arctan\left(\frac{150\times 1.75(0.2-\alpha_s)}{\pi}\right)+0.5 \tag{C14}$$

Appendix D

The BCs for the tangential velocity of the solid phase at the wall developed by Johnson and Jackson[39] are described in Table D1.

Table D1. Johnson and Jackson Semi-Empirical Equations

Tangential velocity at the wall

$$v_{s,w} = -B\frac{\partial v_{s,w}}{\partial n} \tag{D1}$$

where the slip coefficient is given by

$$B = \frac{6\alpha_s.\mu_s}{\sqrt{3}\sqrt{\theta}.\pi.\ \varphi\ .\rho_s g_{0,ss}} \tag{D2}$$

Granular temperature at the wall

$$\theta_w = -C_1\frac{\partial \theta_w}{\partial n} + C_2 \tag{D3}$$

where

$$C_1 = \frac{k\theta_s}{\gamma_w};\ C_2 = \frac{\sqrt{3}\pi\rho_s.u_{s,slip}^2.g_{0,ss}.\theta_s^{3/2}}{6\alpha_{s,max}} \tag{D4}$$

where $u_{s,slip}$, is the slip velocity and accounts for the overall difference between gas and solid velocities.

$$u_{s,slip} = \vec{U}_g - \vec{v}_s \tag{D5}$$

and

$$\gamma_w = \frac{\sqrt{3}\left(1-e_w^2\right)\alpha_s.g_{0,ss}.\theta_s^{3/2}}{4\alpha_{s,max}} \tag{D6}$$

Table D2. Slip BCs Used in the Simulations

Simulation Runs	Friction	Slip Condition	Specularity Coefficient
1	Friction	No-slip	($\varphi = 1$)
2	Partial-friction	Partial-slip	($\varphi = 0.5$)
3	No-friction	Free-slip	($\varphi = 0$)

To assess the effect of BCs on model predictions, simulations have been carried out using different BCs for the solid phase as described in Table D2. In the first set of simulations, the no-slip BC is used with $\varphi = 1$ and the frictional effect of particles on the wall. In the second set of simulations, the partial-slip BC is used ($\varphi = 0.5$) with a partial frictional effect of particles on the wall and, finally, in the third set of simulations, the free-slip BC without particle frictional effect on the wall is studied ($\varphi = 0$). As, a zero specularity coefficient cannot be applied to calculate the slip coefficient in equation (D2) due to mathematical singularity, an equivalent zero shear condition at the wall is applied in the simulations for the free-slip BC.

Manuscript received May 6, 2013, and revision received Jun. 18, 2013.